Author Manuscript

Author Manuscript

Author Manuscript

Author Manuscript

HHS Public Access

Author manuscript

IEEE Trans Biomed Eng. Author manuscript; available in PMC 2019 October 01.

Published in final edited form as:

IEEE Trans Biomed Eng. 2018 October ; 65(10): 2259–2266. doi:10.1109/TBME.2017.2788864.

An adjustable-length Dipole Using Forced-Current Excitation for 7T MR

Jiaming Cui, IEEE [Student Member],

Department of Electrical and Computer Engineering, Texas A&M University, College Station, TX 77843 USA

Ivan E. Dimitrov,

Advanced Imaging Research Center, University of Texas Southwestern Medical Center, Dallas, TX 75390-8568, and Philips Medical Systems, Gainesville, FL 32608, USA.

Sergey Cheshkov,

Advanced Imaging Research Center and the Department of Radiology, University of Texas Southwestern Medical Center, Dallas, TX 75390, USA.

Minyu Gu,

Department of Electrical and Computer Engineering, Texas A&M University, College Station, TX 77843 USA

Craig R. Malloy, and

Advanced Imaging Research Center and the Department of Radiology, University of Texas Southwestern Medical Center, and the VA North Texas Health Care System, Dallas, TX USA.

Steven M. Wright, IEEE [Fellow]

Departments of Electrical and Computer Engineering, Biomedical Engineering and Radiology, Texas A&M University, College Station, TX 77843 USA.

Abstract

Ultra-high field imaging of the body and the spine is challenging due to the large field-of-view (FOV) required. It is especially difficult for RF transmission due to its requirement on both the length and the depth of the B_1^+ field. One solution is to use a long dipole to provide continuous current distribution. The drawback is the natural falloff of the B_1 field towards the ends of the dipole, therefore the B_1^+ per unit square root of maximum specific absorption rate ($B_1^+/\sqrt{SAR_{max}}$) performance is particularly poor towards the end of the dipole. In this study, a segmented element design using forced-current excitation and a switching circuit is presented. The design provides long FOV when desired and allows flexible FOV switching and power distribution without additional power amplifiers. Different element types and arrangements were explored and a segmented dipole design was chosen as the best design. The segmented dipole was implemented and tested on the bench and with a phantom on a 7T whole body scanner. The switchable mode dipole enabled a large FOV in the long mode and improved $B_1^+/\sqrt{SAR_{max}}$ efficiency in a smaller FOV in the short mode.

jm0828@tamu.edu.

Color versions of one or more figures in this paper are available online at http://ieeexplore.ieee.org.

Author Manuscript Author Manuscript Author Manuscript Author Manuscript

Keywords

High field MRI; 7T; dipole; forced-current excitation; SAR; body coil

I. INTRODUCTION

The most useful radiological information that aids a differential spinal lesion diagnosis is the exact location of that lesion with respect to the spinal dura and medulla [1]. MRI at 7T comes with additional SNR gains that can be utilized for improved lesion localization, but its application in the spine has been challenging due to the large field of view (FOV) required which complicates radio frequency (RF) excitation. Recently, alternative approaches to RF transmission based on electric dipole antennas has been explored, and a 37-cm electrical dipole transmit element was demonstrated for spine imaging at 7T [2]. The design provides a large FOV coverage and good RF penetration into the sample.

A common figure of merit in high field RF coil design is the ratio of the effective magnetic flux produced at a point of interest (B_1^+) to the square root of the maximum 10g averaged specific absorption rate (SAR), denoted by $B1^+/\sqrt{SAR_{10g_max}}$ [3–5]. For the 37-cm dipole, the $B_1^+/\sqrt{SAR_{10g_max}}$ is intrinsically low towards the end of the dipole due to its sinusoidal current distribution. To get sufficient B_1^+ towards the ends of the dipole, one may need to use increased power, increasing the local SAR. Therefore, to use a conventional dipole most effectively over the entire FOV, it may be important to increase the $B_1^+/\sqrt{SAR_{10g_max}}$ efficiency at the ends of a long dipole.

Furthermore, in 7T spine imaging it would be desirable to tailor the length of the coil, such that only the desired segment of the spine (e.g. cervical, thoracic or lumbar zone) is excited, while redundant heat deposition into other parts of the spine is avoided. Although achieving an adjustable FOV is possible through the use of multiple power amplifiers and parallel transmission, the method is difficult to scale up beyond certain small number of independent channels [6, 7]. For example, to independently drive an array of six elements, in two sets of three along the length of the spine, six amplifiers would be needed. While eight channel transmit systems are becoming available, they are not common and are very expensive. Even with a multiple transmit system, one still needs to consider decoupling strategies, which can be quite complicated for a dense transmit array [8–20]. To address these challenges, a segmented-element approach that allows adjustable FOV without using extra power amplifiers is proposed in this paper. The method also improves the $B_1^+/\sqrt{SAR_{10g_max}}$ efficiency at the ends of the element.

A segmented dipole that uses PIN diode at various locations along the dipole to alter the FOV has been reported before [21]. The design requires that the dipole be fed from the center of the entire dipole, therefore limiting the FOVs that can be achieved. Previously we have reported a breast coil at 7T that also allows switchable FOV [22, 23] by using forced-current excitation (FCE). The FCE approach ensures equal current delivery to multiple feed points in the array despite mutual coupling, and also enables individual elements to be “turned off” [23]. In this paper, by applying FCE to multiple feed points on the same element, we enable a design that provides both a large FOV with more uniform current

Author Manuscript Author Manuscript Author Manuscript Author Manuscript

distribution than a conventional dipole as well as the ability to move the FOV along the element. The design also improves the $B_1^+/\sqrt{SAR_{10g_max}}$ efficiency at the ends of the element as compared to the conventional dipole. The FCE feeding network contributes its own loss due to impedance mismatch at the element feed points and the standing wave effect on the feed cables[24]. In this case, the loss was found to be approximately 40%, but as this loss is not deposited in the patient it has no impact on $B_1^+/\sqrt{SAR_{10g_max}}$ efficiency of the coil.

Two types of coil element, as potential elements for body and spine imaging, were compared in electromagnetic simulation to optimize the $B_1^+/\sqrt{SAR_{10g_max}}$ efficiency. One of these elements was chosen as the final design and was implemented. It was then tested on the bench and on a phantom in a 7T body scanner.

II. MATERIALS AND METHOD

A. Element comparison

1) General description—The dipole has been shown to have advantages over traditional elements such as loop coils and microstrip coils, in terms of $B_1^+/\sqrt{SAR_{10g_max}}$ efficiency and excitation pattern [3]. When it comes to spine imaging, an element that is sufficiently long along the z-direction (head-to-foot direction) is required. A long dipole, such as the one reported in [2], or a rung element, such as the one reported in [25], are possible candidates. Both elements can be segmented to enable an adjustable FOV. In this design, three selectable segments along the z-direction are used, with each element having their own feed.

The two types of elements, dipole and rung, were modeled and compared using full-wave electromagnetic simulation (XFdtd 7.4, Remcom, State College, PA). For the dipole, a single long dipole was compared to segmented dipoles, for which two configurations were examined: Having three separate short dipoles separated by small gaps; Or having a long dipole with three independent feed locations, allowing adjustable current distributions using FCE. For the rung, due to the spread-out current on a large ground plane that may affect the effective FOV, a single long rung was not examined, but rather three aligned rungs, each fed with FCE, with the same overall length as the long dipole.

To sum up, there are four cases that need to be compared before finalizing the design, as shown in Fig. 1:

- Case 1-Long dipole : A regular 37-cm long dipole [2], with 1.2 cm width and 2 mm gap between the legs, was modeled as the reference.
- Case 2-Segmented rung element: Three separate rungs, each 11.6 cm long and 1.2 cm wide, were modeled. The total length of the structure is also 37 cm, same as reported in [26]. Each rung is 1.2 cm above its ground plane (11.8 cm (z) x 15 cm (x)). Each rung was segmented by 33pF distributed capacitors every 2cm and was fed from the center.

Author Manuscript Author Manuscript Author Manuscript Author Manuscript

- Case 3-Separate dipoles: Three separate dipoles, each 11.6 cm long and 1.2 cm wide, separated by 1.1 cm, was modeled. The total length of the structure is also 37 cm. All dipoles were fed from the middle.
- Case 4-Segmented dipoles: A 37 cm long, 1.2 cm wide dipole was segmented at three equally spaced locations, forming four pieces of conductors separated by three 2 mm gaps. In this case, each shared dipole segment is 18.4 cm. The neighboring dipole elements share a mutual leg. Each dipole is fed from the corresponding gap.

The phantom modeled is 25 × 15 × 40 cm^3 (X x Y x Z), with dielectric constant of 77 and conductivity of 0.6 S/m to approximate human muscle [3]. The phantom is placed 2 cm away in the y direction from the element (Fig. 2). The RF shield in the magnet bore, inside the gradients, is modeled as a cylindrical copper sheet with a diameter of 59 cm and a length of 50 cm.

In cases 2–4, the elements are designed to be driven by forced-current excitation. The FCE method uses quarter-wave transmission lines to connect a common-voltage point to multiple coil elements. The current delivered to the coil elements are equal despite coupling due to mutual impedances and differences in loading. In electromagnetic simulations, the feeds of the elements are modeled as high impedance (1000 ohm) current sources to simulate the forced-current condition. When simulating the coil in modes where only a few elements are used and the others are detuned, the activated elements were fed with the high impedance current source while the detuned elements are left open-circuited at their feeds, which also simulate the detuning capability of the FCE method [23, 27]. In cases 2–4, each element can be turned on or off independently, enabling various modes, as illustrated in Fig. 3. For convenience, we refer to four modes of the seven possible modes, Mode A (feeding at the -z point only), Mode B (z=0 element only), Mode C (+z element only), Mode A+B+C (all elements), as illustrated in Fig. 3.

In each case, B_1^+ was calculated over the central sagittal plane, as is shown in Fig. 2.

2) Comparison between separated and segmented dipole—When using dipoles as the element, one can either have the three short dipoles separated by a short gap (case 3), or have the adjacent dipoles sharing a leg (case 4). The two configurations have their own advantages and drawbacks.

The B_1^+ patterns of these two cases were calculated, and the case 3 design was eliminated from further consideration, as will be explained in the results section.

3) Comparison between rung and dipole—The rung element operates in traditional quasi-static regime by breaking the rung with multiple capacitors to create a more uniform current distribution [25]. The dipole, on the other hand, was often used due to its radiative behavior, though it has a non-uniform current distribution. Therefore, it is expected that the two elements may behave differently in terms of RF penetration and field uniformity.

Author Manuscript Author Manuscript Author Manuscript Author Manuscript

The $B_1^+/\sqrt{SAR_{10g_max}}$ efficiency was compared between the dipole and the rung element along the y direction (i.e. penetration into the body). The comparison was made at the center location (x=z=0) and the two elements was set to Mode B (z=0 element only).

The segmented dipole was chosen as the final design after this comparison, as explained in the results section.

4) Segmented dipole- Comparison between different modes—Once the segmented dipole was chosen as the final design, to evaluate the effectiveness of mode switching, the $B_1^+/\sqrt{SAR_{10g_max}}$ efficiency of the segmented dipole was compared to that of the standard dipole along the z direction at 5 cm depth into the phantom [2] in different modes.

B. Element design and implementation

The segmented dipole is shown in Fig. 4. The segmented dipole is etched on a 0.1'' FR4 board, with 37 cm overall length, 1.2 cm width and three equally-spaced 2 mm gap as feed points. Each feed point connects to a common-voltage point (CVP) through a quarter-wave coaxial cable (EZ-form-141). The common-voltage point (CVP) is modified to a PIN diode switching circuit to enable remote mode switching [23].

The schematic of the switching circuit is provided in Fig. 5. The circuit determines the status (enabled or detuned) of each of the three coils through biasing two PIN diodes for each channel. An external controller takes three digital signals and converts each to two supply signals, providing bias voltage for the two PIN diodes on the switching circuit for each dipole (take D1 and D2 for example). An 'on' signal drives a −5 V, 100 mA supply output and +35 V supply output, which forward biases D1 and reverse biases D2, respectively. D1 connects the quarter-wave feedline to the CVP, while D2 acts as an open circuit and does not affects the RF signal; On the other hand, an 'off' signal drives a +35 V supply output and a −5 V, 100 mA supply output, which reverse biases D1 and forward biases D2, respectively. D1 disconnects the quarter-wave feedline from the CVP, while D2 acts as a short circuit. The quarter-wave transmission line translates the short circuit to an open circuit at the coil feed, detuning that coil [23].

The layout of the switching circuit inevitably creates a phase shift which will impact the FCE condition. The quarter wave coaxial lines, originally calculated as 17.6 cm, required shortening to compensate for this phase shift: The impedance at the CVP was monitored when a floating quarter wave feedline was connected to the switching circuit and an 'on-off-off' control signal was provided to channels A-B-C. The quarter-wave coax line was trimmed until a short circuit impedance was observed on the network analyzer. This process was repeated on all three feed cables.

D2 is designed to detune the unused coil by providing a short circuit at quarter-wave away from the coil. The impedance presented by D2 needs to be adjusted to compensate for the shortened quarter-wave cable, and this was done in a similar manner: The trimmed quarter-wave coax line was connected to the switching circuit while the impedance at the other end of the cable was monitored. An 'off-off-off' control signal was provided to channels A-B-C.

Author Manuscript Author Manuscript Author Manuscript Author Manuscript

An inductor was added in series with D2, and its value was adjusted until an open circuit impedance was observed on the network analyzer. This process was repeated on all three channels.

Capacitively shortened bazooka baluns were integrated onto the quarter-wave coax lines to reduce common mode current on its outside shield [28, 29]. A λ/4 bazooka balun is not used here because the actual length of the FCE feed cables are shorter than 4, as explained above. In order to reduce the coupling to the driven dipoles, the coax cables were arranged so that they are placed on the equal-potential plane of the dipole (transverse plane in this case) whenever possible.

An identical segmented dipole element was later duplicated to target better axial coverage, as in [2]. The spacing between the two coils was set to 6 cm, also according to [2]. Two standard dipoles [2] with the same dimensions were built for comparison.

C. Bench measurement

The square root of SAR is linearly proportional to the electric field, therefore $B_1^+/\sqrt{SAR_{10g_max}}$ efficiency of a coil is essentially a representation of its B_1^+/max E field property [30]. The B_1^+/max E field of a coil is related to the performance of the coil element only, and is independent of its feeding network.

The FCE method introduces extra loss to the coil system due to the standing wave in the feed cables, which is not modeled in the simulation. It needs to be noted that the loss occurs in the feeding network, and does not affect the delivered B_1^+/max E field in the phantom.

The B_1^+/max E field was measured for the segmented dipole in Mode A, Mode B, Mode C, Mode A+B+C and for the reference standard dipole. The measurement was made at 5 cm deep in the phantom (0.6 S/m saline water [3], the same as was used in the simulation) along the z direction, as is indicated in Fig. 9. The B_1 field was measured using a shielded magnetic field probe [31]. The E field was measured using an E-field probe that takes the form of an open-ended coaxial cable [32]. Both measurements required a HP4195A network analyzer. The S_{21} reading for the B field and E field measurement reflects the B/√input_power and E/√input_power efficiency, respectively.

It is still of interest to know how much power is lost through the feeding network, so the B_1^+/√input_power was also characterized for the elements compared, using a shielded magnetic field probe [31]. As opposed to B_1^+/max E, when scaled to the same input power the B_1^+ efficiency acquired is affected by the loss in the feeding network. The difference between the two measurements is the additional loss caused by the FCE network.

D. MR experiment

As mentioned previously, an identical segmented dipole element was added to provide better axial coverage, as is done in [2]. The segmented dipoles were tested with a Philips 7T Achieva system in transmit/receive mode. Each dipole was fed using a FCE network as shown in Fig. 4, and each FCE network was connected to one of the two transmit channels on the system. The dipoles were loaded with 0.6 S/m saline water made into an agar gel

Author Manuscript Author Manuscript Author Manuscript Author Manuscript

phantom with the same dimension as in the simulations. The phantom was placed 2 cm away from the dipoles.

As the two parallel dipoles are driven through a two-channel multi transmit system, the phase and amplitude of each channel can be independently adjusted. For the segmented dipole, the phase of the two channels were adjusted to find the optimum SNR at 5 cm into the phantom when the dipole was in Mode A. Once the optimum phase setting was found, the same setting was used for all modes due to their intrinsic similarity. The same experiment was then repeated for the reference standard dipole set.

The segmented dipoles were tested in four modes-Mode A, Mode B, Mode C, and Mode A +B+C. Mode A+B, Mode A+C and Mode B+C are possible but were not measured. For each mode, sagittal T1-weighted fast gradient echo (THRIVE) images were obtained with the following scan parameters: FOV 300 × 400 × 200 mm (RL x FH x AP), resolution 2 × 2 × 2 mm (overcontiguous), TR/TE/FA: 4.0 ms/0.97 ms/8°, for a total scan time of 58 seconds. The same experiment was then repeated for the reference dipole set, which was also driven through the two-channel multi transmit system.

In order to examine the $B_1^+/\sqrt{\text{input_power}}$ efficiency, a spectroscopic (STEAM) flip angle series experiment was performed on a voxel of 2 × 2 × 2 cm^3 placed 5 cm into the phantom, directly underneath the center of the dipole set (z=x=0). This measurement does take into account the loss in the feeding network, and therefore is expected to be different than the $B_1^+/\sqrt{SAR_{10g_max}}$ results. The experiment was repeated for the standard dipole, the segmented dipole in the long mode (Mode A+B+C) and in the short mode (Mode B). The drive scale (input power) was fixed while the length of the RF excitation pulse was varied to search for the maximum response, which corresponds to a 90-degree flip angle. The TR used between RF pulses is 5 second to allow complete T1 relaxation.

III. RESULTS AND DISCUSSION

A. Element comparison

1) Comparison between separated or segmented dipole—Initially the two different dipole configurations, separate (case 3) and segmented (case 4), were compared in Mode A+B+C. The calculated B_1^+ patterns in the central sagittal plane are shown in (Fig. 6). The results are scaled to 1W input power

From these simulations, the B_1^+ field of the segmented dipole appears more uniform. The separate dipole configuration has current nulls between the short dipoles and therefore has more inhomogeneous field pattern along the z direction. Based on these results we selected the segmented dipole configuration over the separate dipole configuration for superior B_1^+ pattern. However, it is worth noting that the separate design allows more focused power deposition in the short modes (Mode A, Mode B, Mode C), and therefore can achieve higher $B_1^+/\sqrt{SAR_{10g_max}}$ efficiency in local areas. Should the highest $B_1^+/\sqrt{SAR_{10g_max}}$ efficiency be desired in certain cases, the separate dipole configuration can still be a viable option.

Author Manuscript Author Manuscript Author Manuscript Author Manuscript

2) Comparison between rung and dipole—We next compared the dipole (case 4) and rung element (case 2). $B_1^+/\sqrt{SAR_{10g_max}}$ efficiency vs. depth of case 2 and 4, operated in Mode B was compared along a center line extending into the phantom, as marked in Fig. 7.

The $B_1^+/\sqrt{SAR_{10g_max}}$ efficiency profile along the y direction vs. depth of the rung element is significantly lower, especially at deeper locations (Fig. 8). This is likely due to the current return path provided by the ground plane and the resultant partial B_1^+ field cancellation.

Based on this simulation result, the segmented dipole was chosen as the final configuration for the switchable transmit element.

3) Segmented dipole- Comparison between different modes—The segmented dipole was chosen as the final design. A $B_1^+/\sqrt{SAR_{10g_max}}$ comparison was made in the z direction between all modes (Mode A, B, C, and Mode A+B+C) and the standard dipole. For reference, a full sagittal plane is shown in Fig. 9, with the height for the profile comparison indicated by a dashed line. The profile comparison is shown in Fig. 10

The advantage of using a segmented design where each short element can be turned on and off, is clear from Fig. 10. When switched to Mode A or C, the segmented design provides 0~4 dB higher $B_1^+/\sqrt{SAR_{10g_max}}$ efficiency than the standard dipole in the corresponding area.

B. Bench measurement

A quick S_{21} measurement on the segmented dipole shows a high coupling factor between segments: −13.3 dB between segments A and C, and −7.6 dB between segments A and B. This addresses the importance of using FCE in this design, which allows equal current delivery to the segments despites high coupling [23, 24].

The B_1^+/(max E-field) and $B_1^+/\sqrt{\text{input power}}$ was measured for the segmented dipole in its long (A+B+C) mode, and was compared to that of the reference dipole. The difference was found to be 2.2 dB (40%). This is the additional loss brought by the FCE feeding network. This presents a challenge where available power becomes the limiting factor but as previously discussed it is irrelevant to the $B_1^+/\sqrt{SAR_{10g_max}}$ or B_1/(max E-field) performance.

The B_1^+/(max E-field) measurement is shown in Fig. 11. In general, the comparison between the segmented dipole and the regular dipole corresponds well to the calculated $B_1^+/\sqrt{SAR_{10g_max}}$ results shown in Fig. 10. Due to the natural fall-off of the B_1^+ around the end of the regular long dipole, the segmented dipole in its short modes exhibits 0~4 dB higher efficiency in the local area than the standard dipole. When set to the long mode, the segmented dipole has a flatter but longer profile along the z direction (head-to-foot) than the regular dipole.

It is also clear from these measurements that when operated in its short mode, the other part of the segmented dipole is well detuned. The residual signal around the ends of the dipoles is due to the finite quality factor of the detuning circuit, but is at least 20 dB below the

Author Manuscript Author Manuscript Author Manuscript Author Manuscript

maximum signal. Therefore, unnecessary power deposition into the unwanted area can be avoided when using the segmented dipole.

C. MR experiment

The segmented dipole has adjustable FOV and a large coverage in its long mode in the z direction. However, its axial coverage may be insufficient for in vivo spine imaging. Having two segmented dipoles side by side in the x direction and separated by 6 cm, driven by two independent transmit channels greatly improves the axial FOV. In optimizing the transmit phase for the two channels, it was found that the maximum signal intensity at 5 cm into the phantom occurs with the phase setting of 0 and 90, which is in good agreement with the results presented in [2]. This applies to both the standard dipole and the segmented dipole. The improved axial coverage when driving two segmented dipoles simultaneously is seen on the MRI image in Fig. 12.

The THRIVE images obtained in central sagittal plane with this configuration are shown in Fig. 13.

The axial images demonstrate good axial coverage in multi-transmit configuration. The sagittal images in different modes demonstrate the mode-switching capability. In the long mode, a large coverage in the z direction was obtained, which is sufficient for covering the required anatomy on the typical T2w sagittal spine images. In short modes, the ability to smoothly shift the FOV is observed, and the unused segments are successfully detuned.

The spectroscopic flip angle series calibrating for a 90-degree flip angle at 5cm deep was performed with the segmented dipole (in long mode and in short mode) and compared to the standard dipole. For this experiment, the drive scale (input power) was fixed while the length of the RF excitation pulse was linearly increased to search for the maximum response in each case, giving a series of response spectra. With a coil of higher $B_1^+/\sqrt{\text{input_power}}$ efficiency, the maximum response (90-degree flip angle) would occur with a shorter RF pulse, at an earlier stage of the flip angle series. The result is presented in Fig. 14.

To reach 90 degree flip angle, the segmented dipole in the long mode takes 1.5 times the duration of that in the short mode as well as the standard dipole. It can then be calculated that: At the voxel compared, the $B_1^+/\sqrt{\text{input_power}}$ efficiency of the regular dipole is similar to that of the segmented dipole in short mode, and is 1.5 times (3.5 dB) higher than that of the segmented dipole in long mode. This difference includes the loss in the FCE network, and therefore is not equivalent to the $B_1^+/\sqrt{SAR_{10g_max}}$ comparisons, which was presented in Fig. 10.

IV. CONCLUSIONS

Long dipoles have been used for spine imaging at 7T. The low $B_1^+/\sqrt{SAR_{10g_max}}$ efficiency towards the end of the dipole calls for a flexible design where segments of a long structure can be turned on and off to manipulate the power distribution.

In this work, several design options for a switchable FOV, long element targeted for 7T spine imaging were compared in simulation. A long dipole, segmented into three smaller dipoles

Author Manuscript Author Manuscript Author Manuscript Author Manuscript

where adjacent dipoles share a mutual leg, was chosen as the final design. The flexible design allows higher $B_1^+/\sqrt{SAR_{10g_max}}$ towards the end of the dipole, with the drawback being the reduced $B_1^+/\sqrt{input_power}$ efficiency in its long mode. The segmented dipole was implemented by utilizing forced-current excitation and a PIN-diode switching circuit. Each segment of the dipole can be activated or detuned by an electronic control. The design of the FCE configuration and the switching circuit layout is independent of the coil element used. In other words, one can use any coil element desired and still be able to implement this technique. In this case, a segmented dipole configuration was selected to obtain uniform excitation and continuous FOV switching, which are of great significance in clinical spine imaging.

The segmented dipole was evaluated on bench and on a phantom in a 7T whole body scanner. It was also compared to the standard dipole that has been published [2]. While the FCE feeding network does bring an extra loss to the segmented dipole, especially in the long mode, the loss is contained in the circuit instead of the phantom, and therefore does not affect the $B_1^+/\sqrt{SAR_{10g_max}}$ efficiency. The next step is to investigate methods to improve the raw $B_1^+/\sqrt{input_power}$ efficiency, which may require the use of lower loss coaxial cables or partially matching the dipoles before the $\lambda/4$ cables. Further implementation of receive arrays is expected to improve sensitivity.

Acknowledgments

This work is supported by CPRIT Grant RP160847 and NIH Grant EB015908.

REFERENCES

[1]. Edelman RR et al., Clinical Magnetic Resonance Imaging 3rd Edition, pp. 2159, 2006.

[2]. Duan Q et al., “A 7T spine array based on electric dipole transmitters,” Magnetic Resonance in Medicine, vol. 74, no. 4, pp. 1189–1197, 2015. [PubMed: 26190585]

[3]. van den Bergen B et al., “Uniform prostate imaging and spectroscopy at 7 T: comparison between a microstrip array and an endorectal coil,” NMR in Biomedicine, vol. 24, no. 4, pp. 358–365, 2011. [PubMed: 20960577]

[4]. Raaijmakers AJ et al., “The fractionated dipole antenna: A new antenna for body imaging at 7 Tesla,” Magnetic Resonance in Medicine, 2015.

[5]. Raaijmakers A et al., Dipole antennas for ultrahigh field body imaging: a comparison with loop coils, NMR in Biomedicine, 2015.

[6]. Katscher U, and B¶rnert P, “Parallel RF transmission in MR,” NMR in Biomedicine, vol. 19, no. 3, pp. 393–400, 2006. [PubMed: 16705630]

[7]. Wiesinger F et al., “ Potential and feasibility of parallel MRI at high field,” NMR in Biomedicine, vol. 19, no. 3, pp. 368–378, 2006. [PubMed: 16705638]

[8]. Von Morze C et al., An eight channel, nonoverlapping phased array coil with capacitive decoupling for parallel MRI at 3 T,” Concepts in Magnetic Resonance Part B: Magnetic Resonance Engineering, vol. 31, no. 1, pp. 37–43, 2007.

[9]. Jevtic J, “Ladder networks for capacitive decoupling in phased-array coils.” Proc. Intl Soc Mag Reson Med, p. 2001, 2017.

[10]. Lee RF et al., “Coupling and decoupling theory and its application to the MR phased array,” Magnetic Resonance in Medicine, vol. 48, no. 1, pp. 203–213, 2002. [PubMed: 12111947]

[11]. Li Y et al., “ ICE decoupling technique for RF coil array designs,” Medical Physics, vol. 38, no. 7, pp. 4086–4093, 2011. [PubMed: 21859008]

Author Manuscript Author Manuscript Author Manuscript Author Manuscript

[12]. Wu B et al., Interconnecting L/C components for decoupling and its application to low field open MRI array, Concepts in Magnetic Resonance Part B: Magnetic Resonance Engineering, vol. 31, no. 2, pp. 116–126, 2007.

[13]. Avdievich NI et al., “Resonant inductive decoupling (RID) for transceiver arrays to compensate for both reactive and resistive components of the mutual impedance,” NMR in Biomedicine, vol. 26, no. 11, pp. 1547–1554, 2013. [PubMed: 23775840]

[14]. Connell IR et al., “MR RF array decoupling method with magnetic wall distributed filters,” IEEE Transactions on Medical Imaging, vol. 34, no. 4, pp. 825–835, 2015. [PubMed: 25838388]

[15]. Kurpad KN et al., “RF current element design for independent control of current amplitude and phase in transmit phased arrays,” Concepts in Magnetic Resonance Part B: Magnetic Resonance Engineering, vol. 29, no. 2, pp. 75–83, 2006.

[16]. Chu X et al., Ultra low output impedance RF power amplifier for parallel excitation,” Magnetic Resonance in Medicine, vol. 61, no. 4, pp. 952–961, 2009. [PubMed: 19189287]

[17]. Hoult D et al., “The MR multi-transmit phased array: a Cartesian feedback approach,” Journal of Magnetic Resonance, vol. 171, no. 1, pp. 64–70, 2004. [PubMed: 15504683]

[18]. Gudino N, and Griswold MA, Multi Turn Transmit Coil to Increase B1 Efficiency in Current Source Amplification, Magnetic Resonance in Medicine, vol. 69, no. 4, pp. 1180–1185, 2013. [PubMed: 23401060]

[19]. Adriany G et al., “Transmit and receive transmission line arrays for 7 Tesla parallel imaging,” Magnetic Resonance in Medicine, vol. 53, no. 2, pp. 434–445, 2005. [PubMed: 15678527]

[20]. Zhang X et al., “An inverted-microstrip resonator for human head proton MR imaging at 7 tesla,” IEEE Transactions on Biomedical Engineering, vol. 52, no. 3, pp. 495–504, 2005. [PubMed: 15759580]

[21]. Duan Q et al., “Segmented Dipole: A Remotely Reconfigurable Near-Field Dipole Antenna Transmitter for Optimized 7 T Spine maging,” Pro Intl Soc Mag Reson Med, vol. 3512, 2016.

[22]. Cui J et al., “Switchable bilateral unilateral 7T breast coil using forced current excitation,” Pro Intl Soc Mag Reson Med, vol. 2727, 2013.

[23]. Cui J et al., “A Switched-Mode Breast Coil for 7 T MRI Using Forced-Current Excitation,” IEEE Transactions on Biomedical Engineering, vol. 62, no. 7, pp. 1777–1783, 2015. [PubMed: 25706501]

[24]. McDougall MP et al., “A simple approach to overcoming mutual coupling effects in some transmit array coils for magnetic resonance imaging.” pp. 2043–2046. Proc. IEEE Engineering in Medicine and Biology Conference, 2008.

[25]. Moody KL et al., “An eight-channel T/R head coil for parallel transmit MRI at 3T using ultra-low output impedance amplifiers,” Journal of Magnetic Resonance, vol. 246, pp. 62–68, 9//, 2014. [PubMed: 25072190]

[26]. Cui J et al., “An adjustable field-of-view rung element for 7T transmit array coils using forced current excitation,” Pro Intl Soc Mag Reson Med, vol. 2673, 2017.

[27]. By S et al., “A 16-Channel Receive, Forced Current Excitation Dual-Transmit Coil for reast maging at 7T,” PloS one, vol. 9, no. 11, pp. e113969, 2014. [PubMed: 25420018]

[28]. Dieringer MA et al., “Design and application of a four-channel transmit receive surface coil for functional cardiac imaging at 7T,” Journal of Magnetic Resonance Imaging, vol. 33, no. 3, pp. 736–741, 2011. [PubMed: 21438067]

[29]. Kriegl R et al., “ Novel inductive decoupling technique for flexible transceiver arrays of monolithic transmission line resonators,” Magnetic Resonance in Medicine, vol. 73, no. 4, pp. 1669–1681, 2015. [PubMed: 24753115]

[30]. Jin J, Electromagnetic analysis and design in magnetic resonance imaging, Boca Raton, Florida: CRC press, 1998.

[31]. Alecci M et al., “Radio frequency magnetic field mapping of a 3 Tesla birdcage coil: Experimental and theoretical dependence on sample properties,” Magnetic Resonance in Medicine, vol. 46, no. 2, pp. 379–385, 2001. [PubMed: 11477643]

[32]. Baudry D et al., “Characterization of the open-ended coaxial probe used for near-field measurements in EMC applications,” Progress In Electromagnetics Research, vol. 60, pp. 311–333, 2006.

Author Manuscript

Author Manuscript

Author Manuscript

Author Manuscript

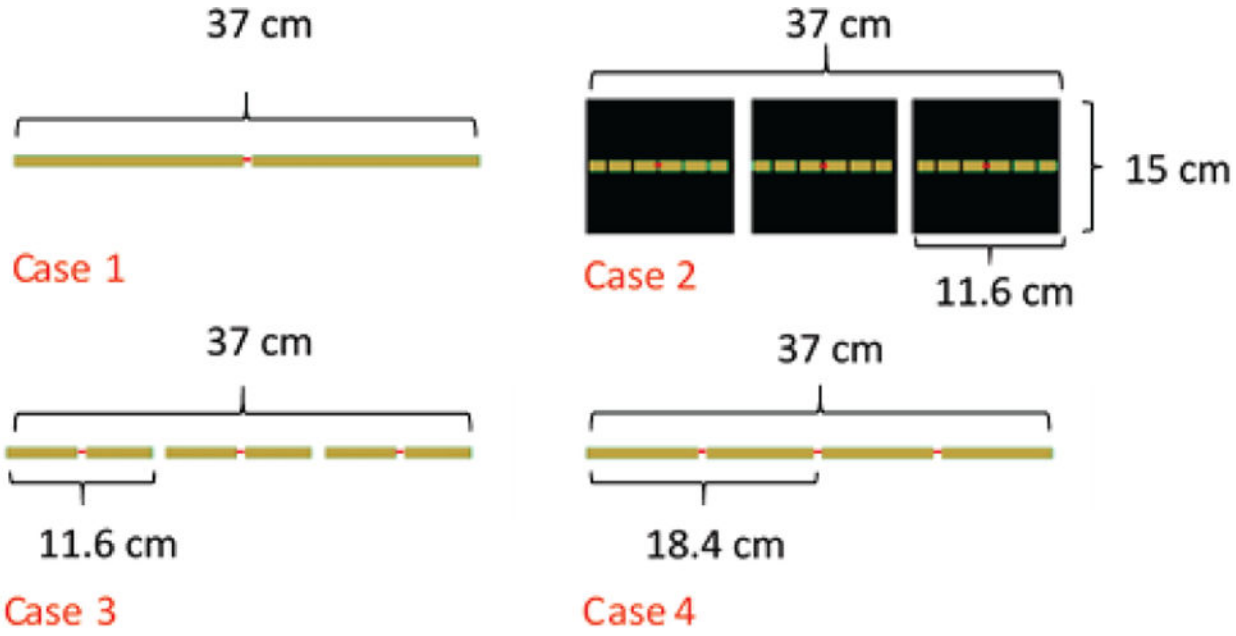

Fig. 1.

Four different designs with the same overall length (37 cm), top view. Case 1: standard dipole; Case 2: separate rungs (ground is displayed as black); Case 3: separate dipoles; Case 4: segmented dipole. The feed locations in each case are marked in red.

Author Manuscript Author Manuscript Author Manuscript Author Manuscript

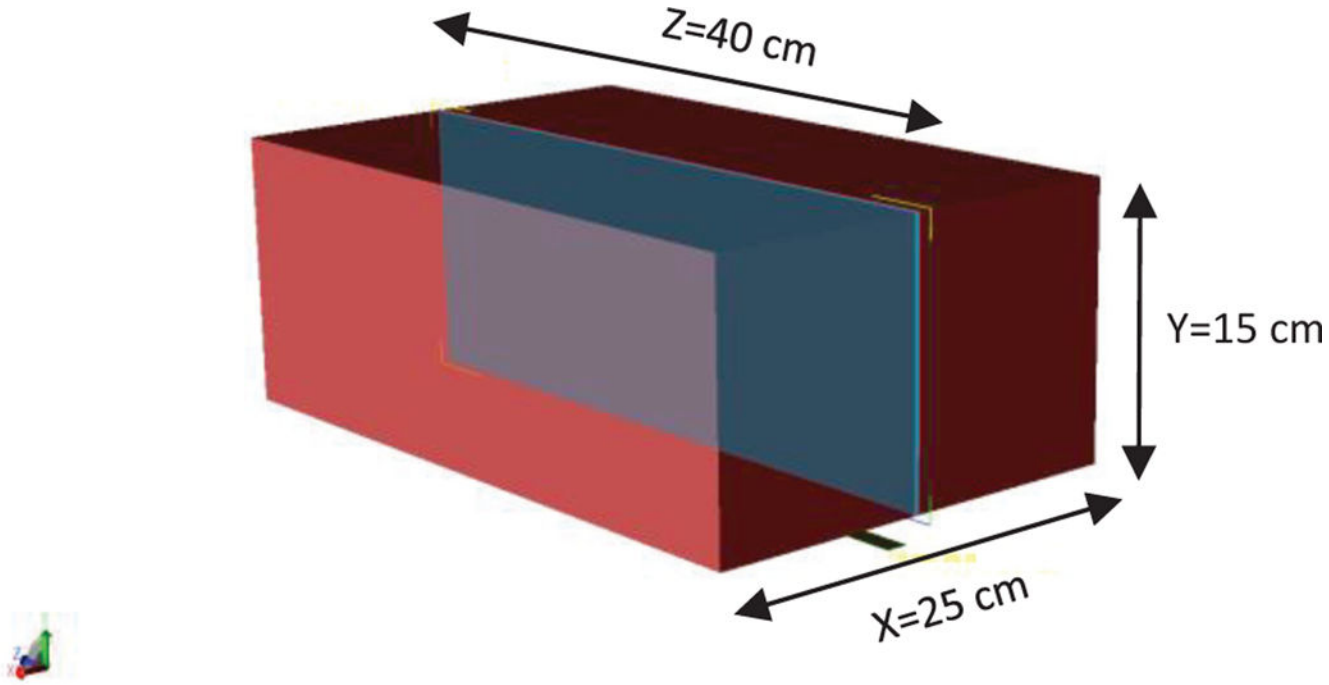

Fig. 2.

Phantom model, and the sagittal plane (in blue) where B_1^+ is calculated. The bore of the magnet is modeled but not displayed.

Author Manuscript Author Manuscript Author Manuscript Author Manuscript

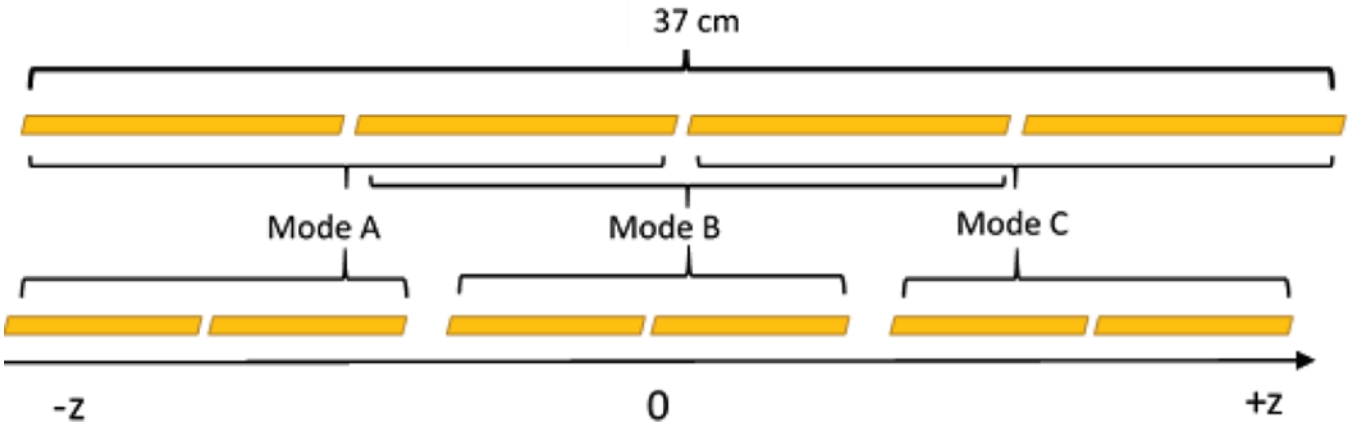

Fig. 3.

Mode definition for segmented (case 4, upper panel) and separated (case 2 and 3, lower panel) configurations

Author Manuscript Author Manuscript Author Manuscript Author Manuscript

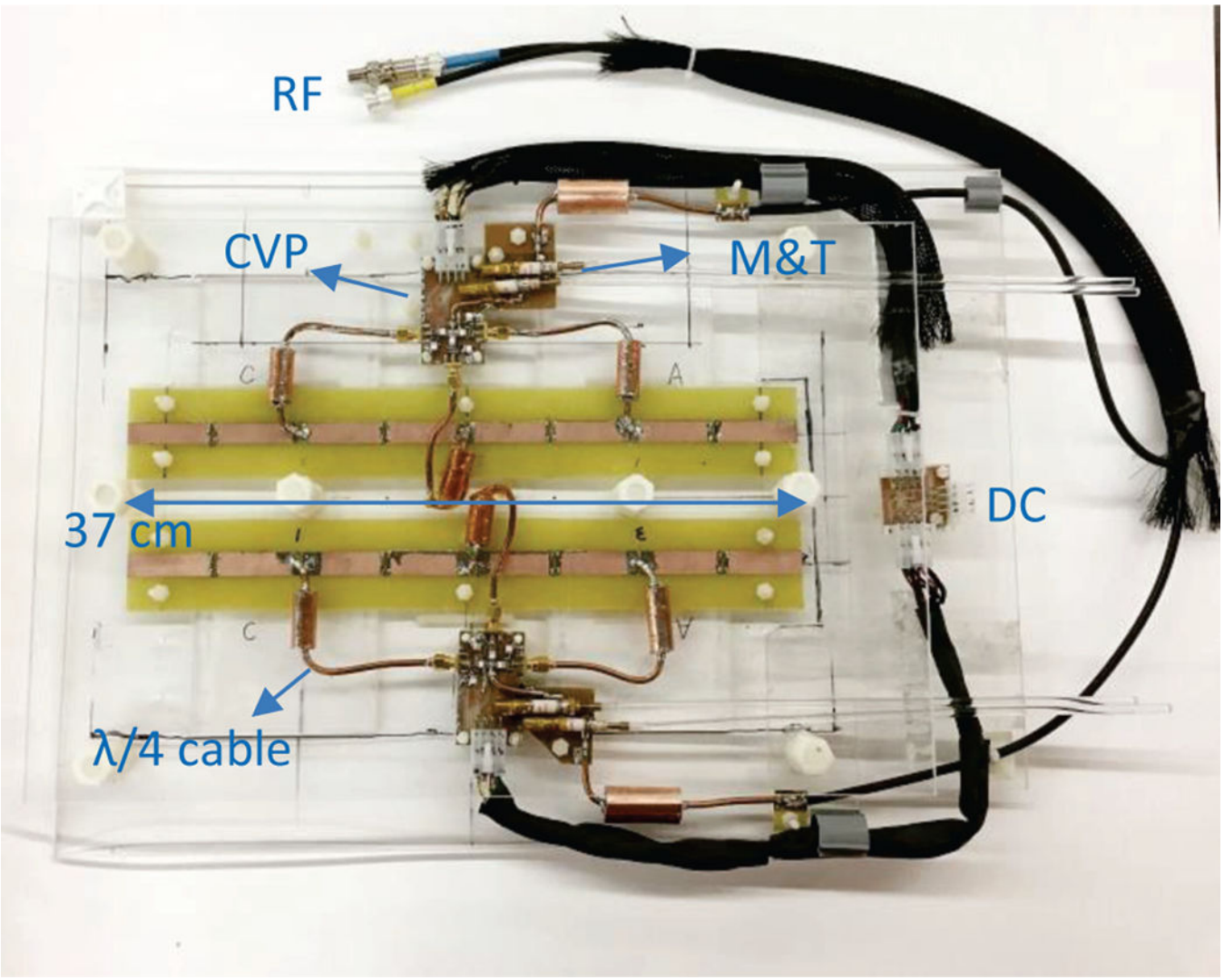

Fig. 4.

Layout of the coil, including dipole, the quarter-wave feedlines with baluns incorporated, the switching networks as well as the matching circuits (marked as M&T)

Author Manuscript

Author Manuscript

Author Manuscript

Author Manuscript

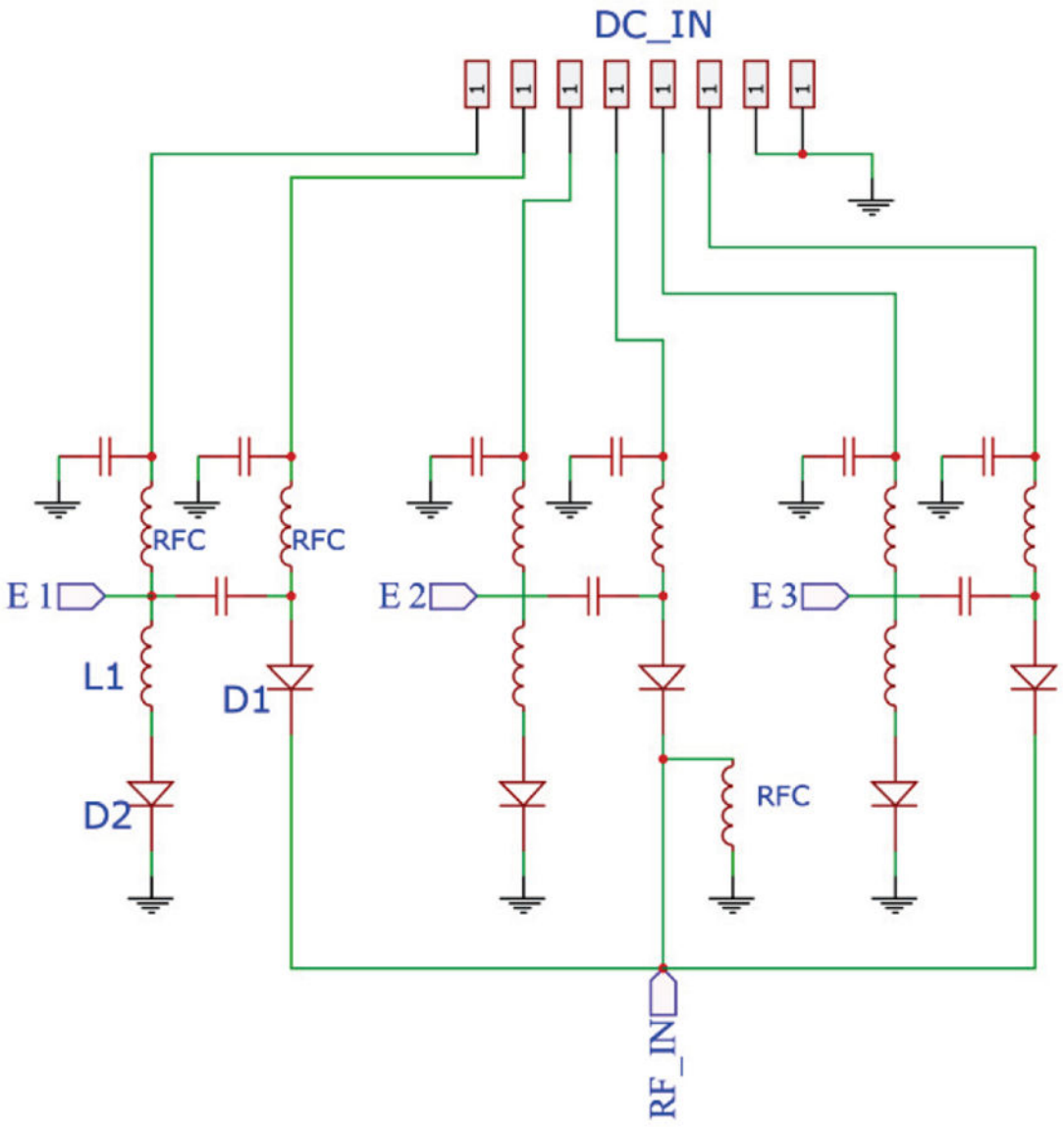

Fig. 5.

Schematic of the switching circuit. 'RFC' stands for RF choke, and 'E1~3' stands for element 1~3.

Author Manuscript

Author Manuscript

Author Manuscript

Author Manuscript

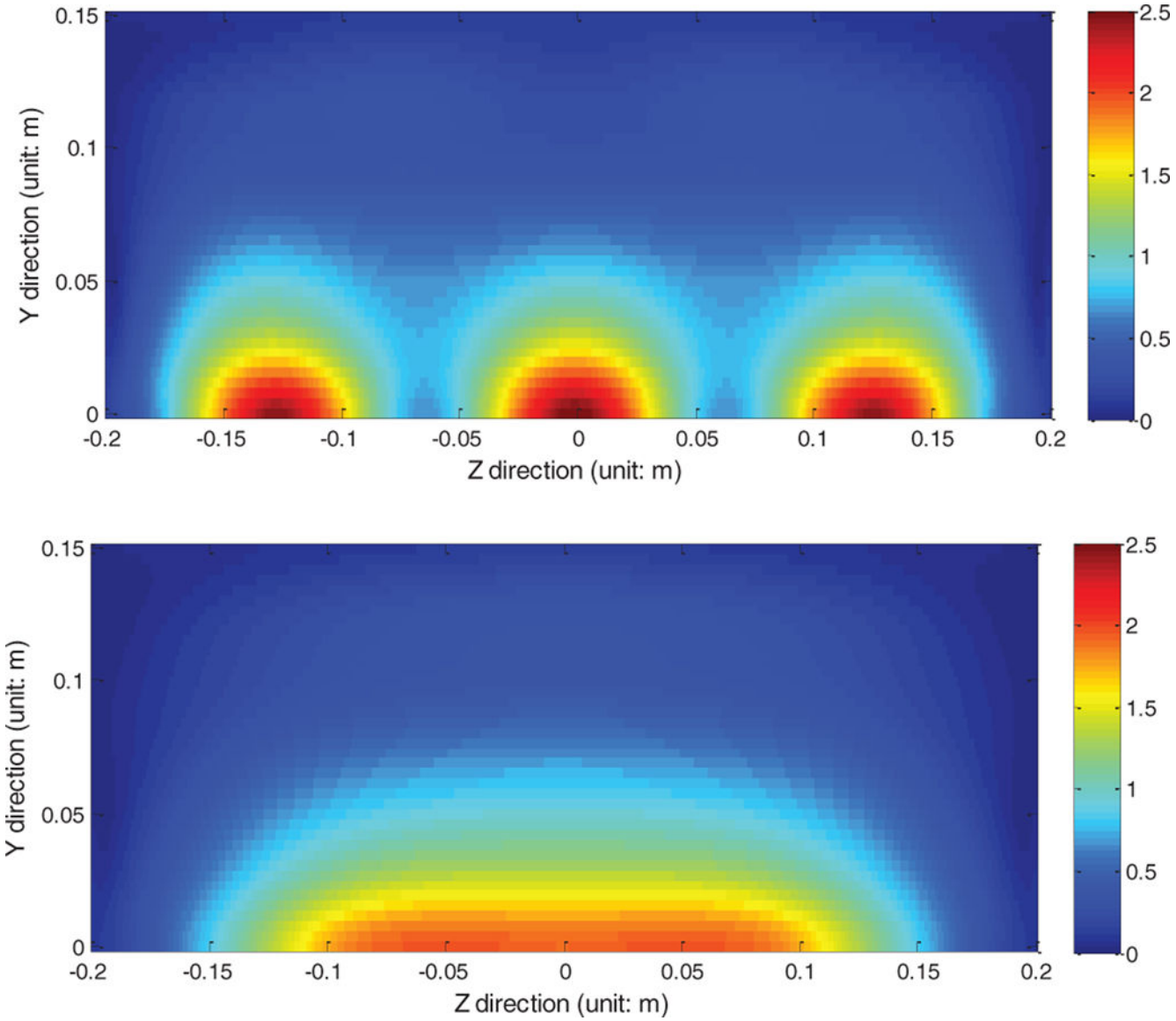

Fig. 6.

(Top) Calculated B_1^+ pattern (in μT) of the separate dipoles (case 3) and (Bottom) the segmented dipole (case 4). In Mode A+B+C, the segmented dipole provides a more uniform excitation pattern than the separate dipoles.

Author Manuscript Author Manuscript Author Manuscript Author Manuscript

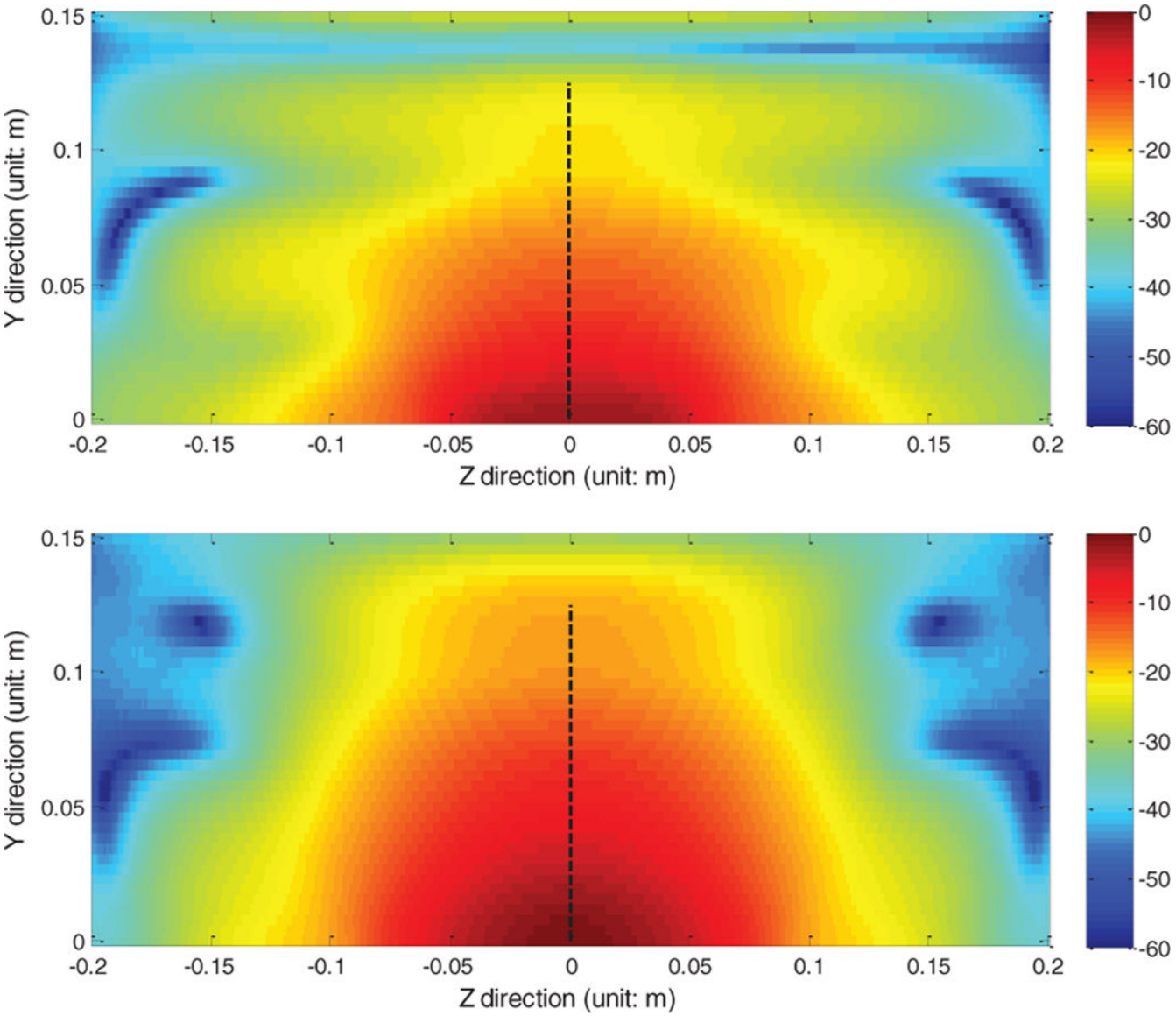

Fig. 7.

Calculated $B_1^+/\sqrt{SAR_{10g_max}}$ pattern of the separate rung (Top) and the segmented dipole (Bottom) in the central sagittal plane. The y direction profiles where $B_1^+/\sqrt{SAR_{10g_max}}$ efficiency was compared are marked with a dashed black line

Author Manuscript Author Manuscript Author Manuscript Author Manuscript

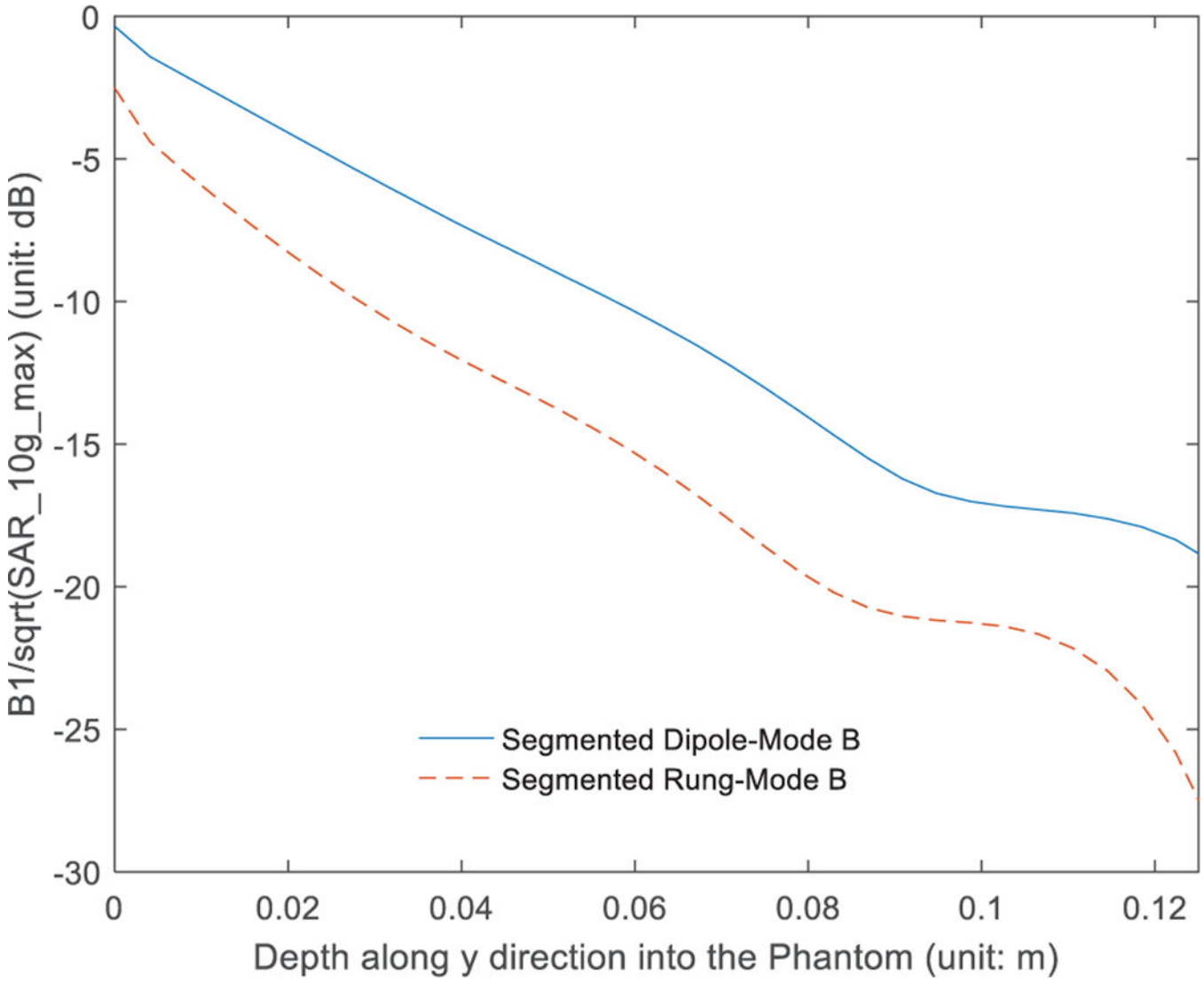

Fig. 8.

Calculated $B_1^+/\sqrt{SAR_{10g_max}}$ efficiency comparison between the separated rung (Mode B) and the segmented dipole (Mode B). The profile position being compared is shown in Fig. 7.

Author Manuscript Author Manuscript Author Manuscript Author Manuscript

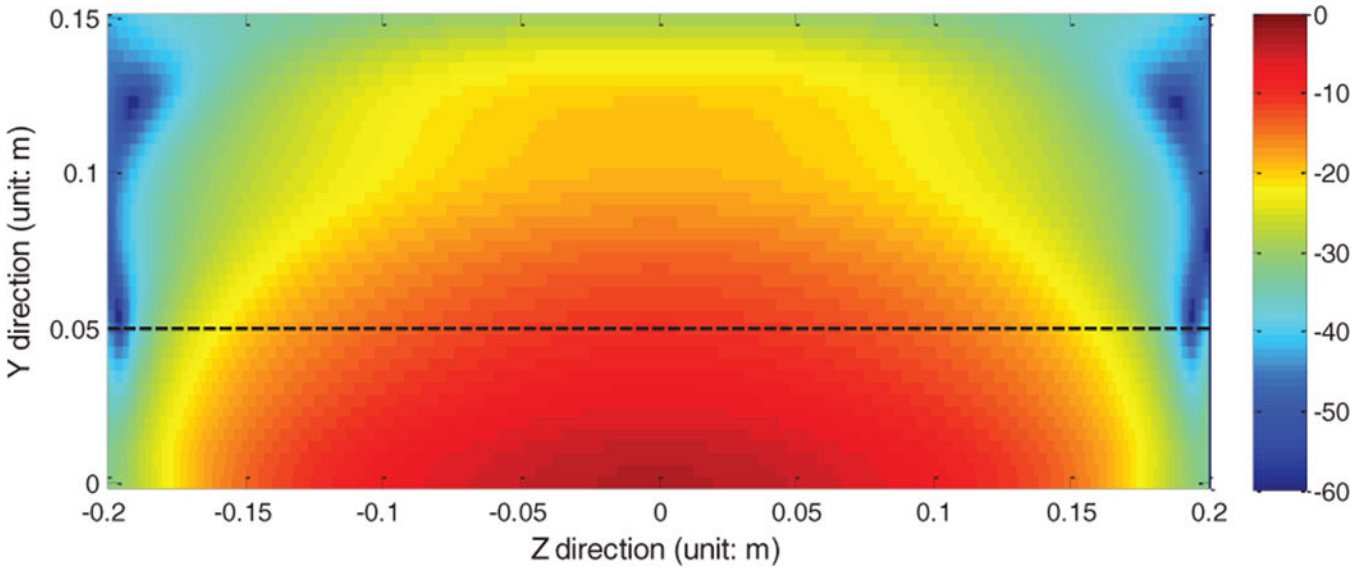

Fig. 9.

Z direction profile being compared as marked in the calculated $B_1^+/\sqrt{SAR_{10g_max}}$ pattern of the reference standard dipole

Author Manuscript Author Manuscript Author Manuscript Author Manuscript

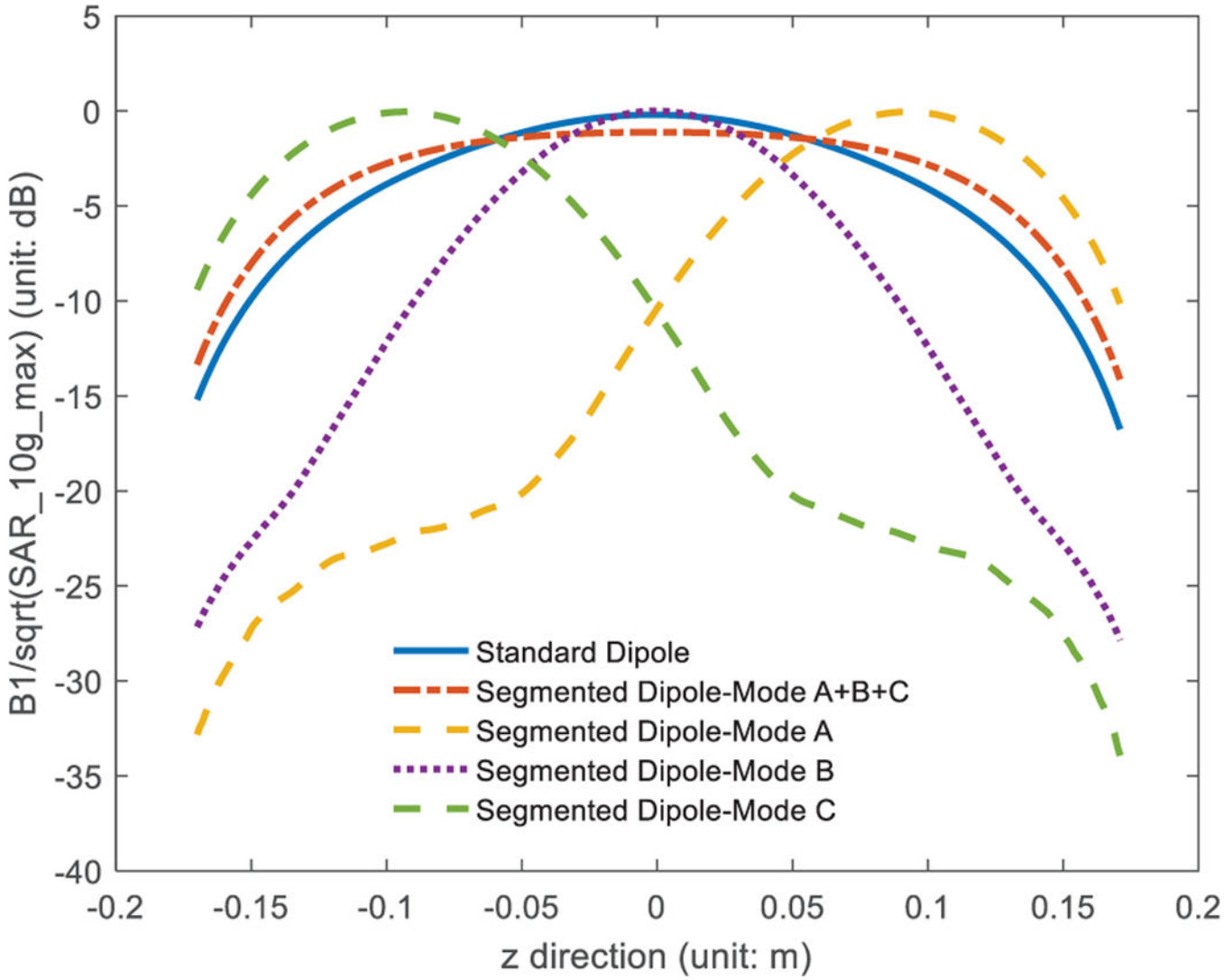

Fig. 10.

Calculated z direction profile comparison between the segmented dipole in different modes and the standard dipole at 5cm deep. The ability to switch FOV is observed.

Author Manuscript Author Manuscript Author Manuscript Author Manuscript

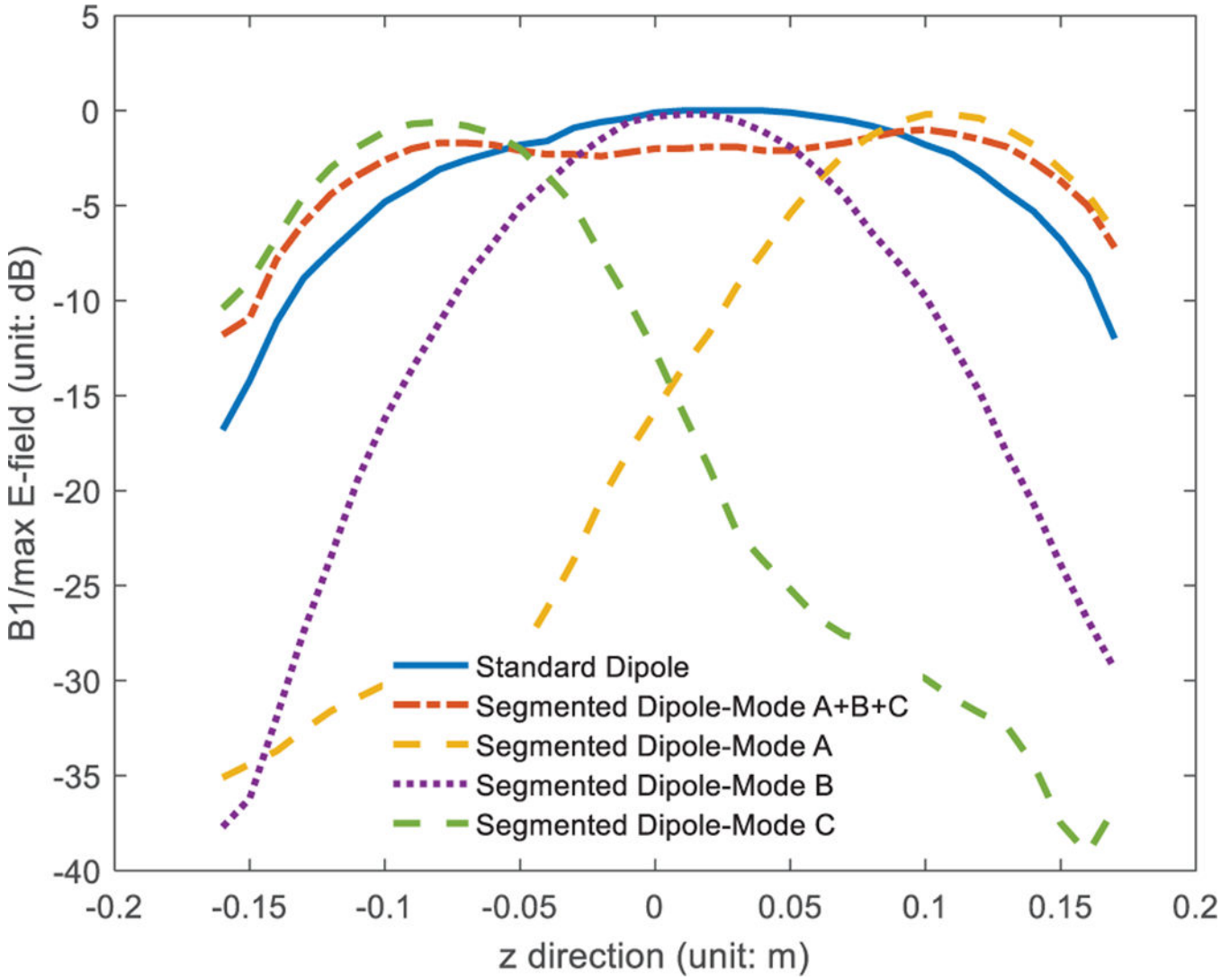

Fig. 11.

B_1^+/max E results measured on bench at 5cm into the phantom. Comparison was made between the segmented dipole in different modes and the standard dipole

Author Manuscript Author Manuscript Author Manuscript Author Manuscript

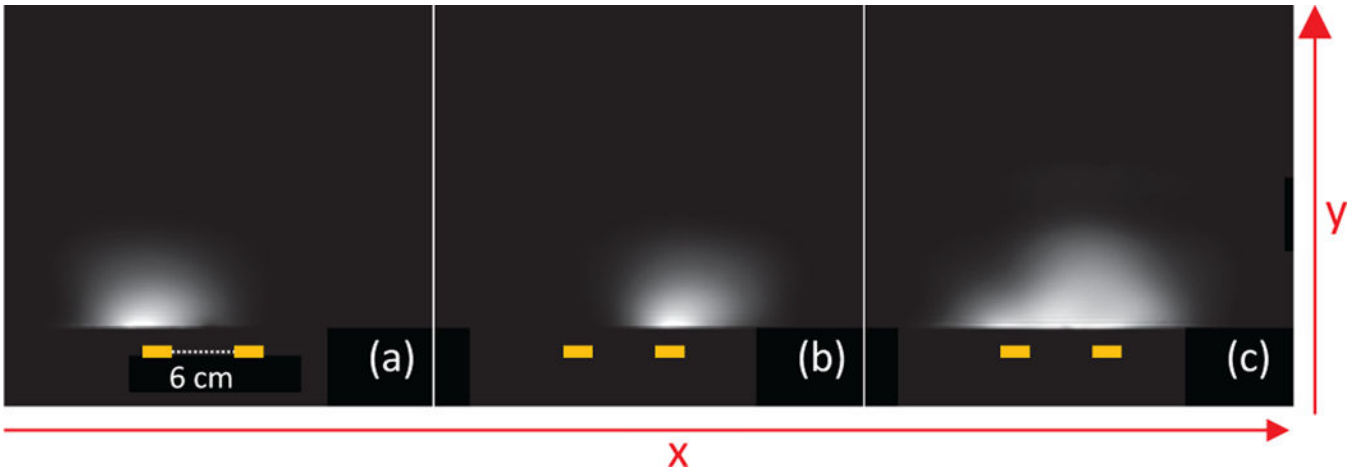

Fig. 12.

(a) Axial image from segmented dipole element #1 (b) Axial image from segmented dipole element #2 (c) Axial image from two segmented dipoles transmitting at the same time. When two dipoles are used, the axial coverage is improved. The locations of the dipoles are marked with yellow squares.

Author Manuscript

Author Manuscript

Author Manuscript

Author Manuscript

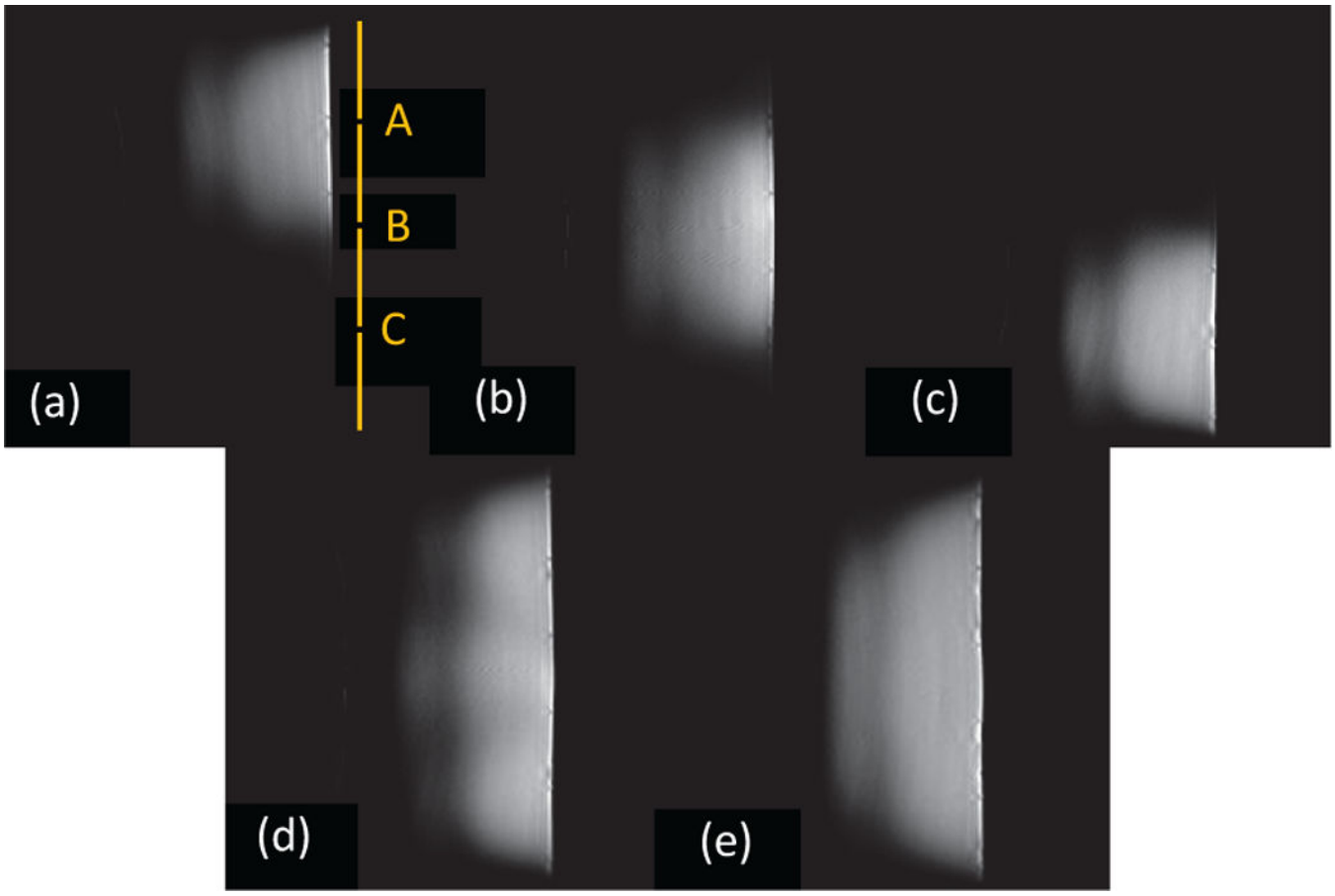

Fig. 13.

Sagittal THRIVE images from the segmented dipoles (a-d) and the reference standard dipoles (e): (a) Segmented dipoles-Mode A. (b) Segmented dipoles-Mode B. (c) Segmented dipoles-Mode C. (d) Segmented dipoles-Mode A+B+C. (e) Reference regular dipoles. For the segmented dipole, in long mode, long coverage in z direction is achieved; In short mode, the ability to switch FOV is observed and the unused segments are successfully detuned. The location of the dipole is marked as yellow lines.

Author Manuscript Author Manuscript Author Manuscript Author Manuscript

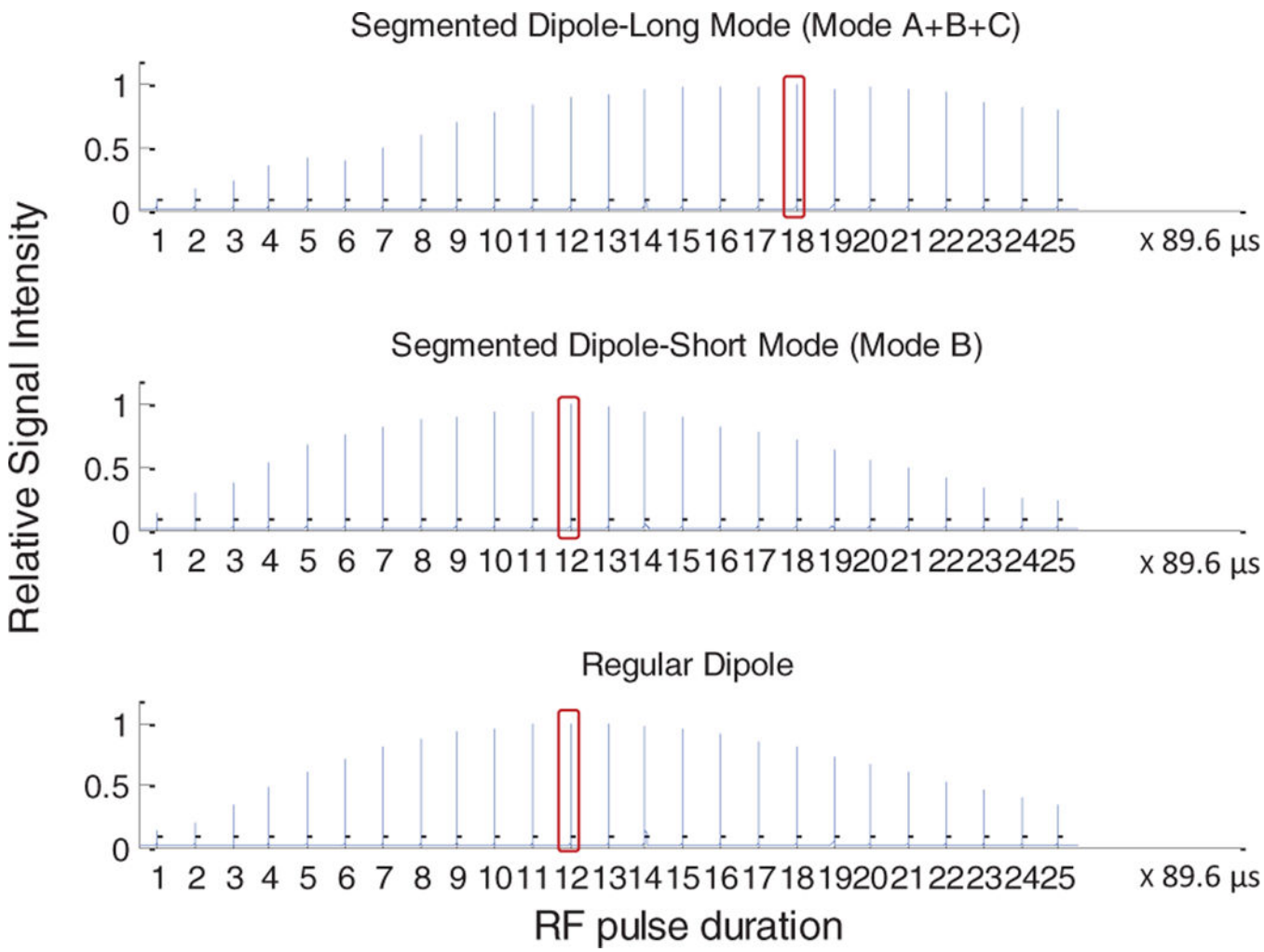

Fig. 14.

Flip angle series experiment performed on the segmented dipole and the standard dipole. Horizontal axis indicates the multiples of unit pulse length. The length of the RF pulse is linearly proportional to the pulse number. The maximum signal corresponds to a 90-degree flip angle, and is marked with a red circle.